iScience

CellPress

Article

Grafting Cobalt Diselenide on Defective Graphene for Enhanced Oxygen Evolution Reaction

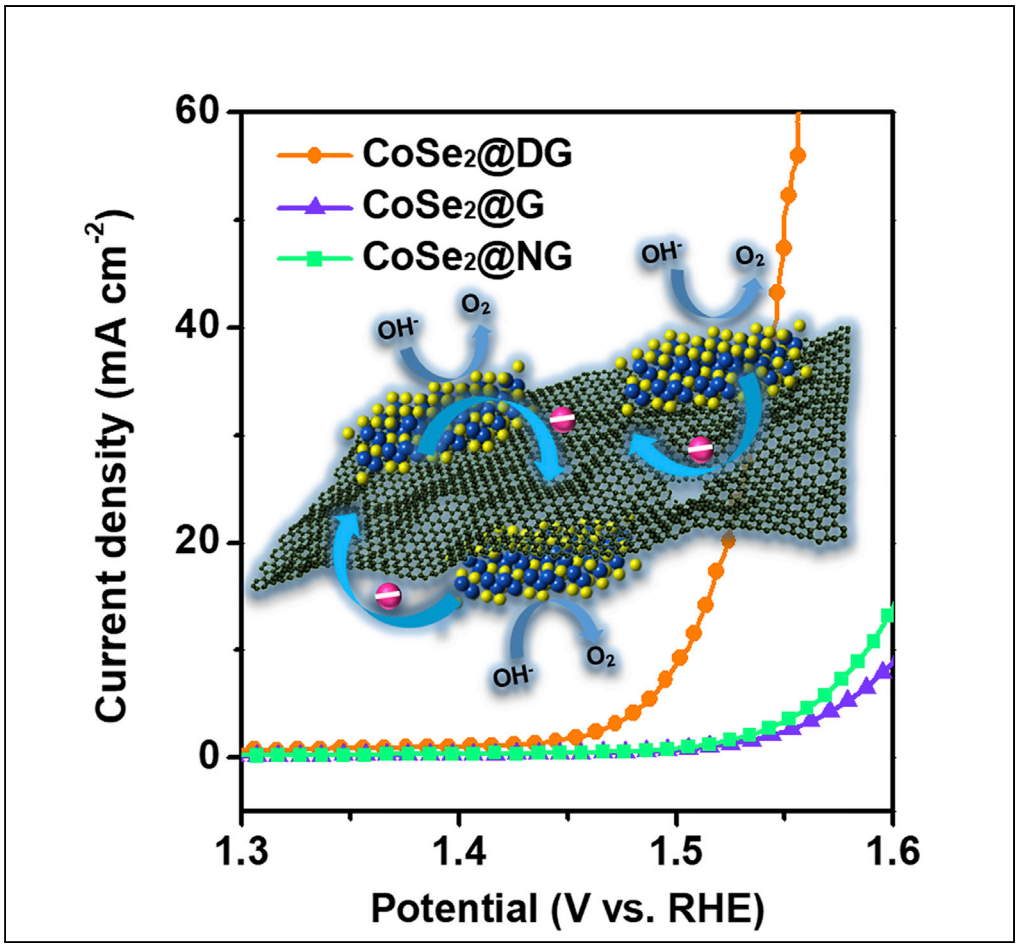

Xin Wang, Linzhou Zhuang, Tianwei He, ..., Zhonghua Zhu, Xiangdong Yao, Shu-Hong Yu

x.yao@griffith.edu.au (X.Y.)
shyu@ustc.edu.cn (S.-H.Y.)

HIGHLIGHTS

A hybrid catalyst with in-plane $CoSe_2$/defective graphene heterostructures

The catalyst exhibits an excellent and stable oxygen evolution reaction (OER) activity

Enhanced OER performance is due to the synergy of exposed cobalt atoms and carbon defects

Wang et al., iScience 7, 145–153
September 28, 2018
https://doi.org/10.1016/j.isci.2018.08.013

iScience

CellPress

Article

Grafting Cobalt Diselenide on Defective Graphene for Enhanced Oxygen Evolution Reaction

Xin Wang,[1,2,5] Linzhou Zhuang,[3,5] Tianwei He,[4] Yi Jia,[2] Longzhou Zhang,[2] Xuecheng Yan,[2] Minrui Gao,[1] Aijun Du,[4] Zhonghua Zhu,[3] Xiangdong Yao,[2,*] and Shu-Hong Yu[1,6,*]

SUMMARY

Cobalt diselenide ($CoSe_2$) has been demonstrated to be an efficient and economic electrocatalyst for oxygen evolution reaction (OER) both experimentally and theoretically. However, the catalytic performance of up-to-now reported $CoSe_2$-based OER catalysts is still far below commercial expectation. Herein, we report a hybrid catalyst consisting of $CoSe_2$ nanosheets grafted on defective graphene (DG). This catalyst exhibits a largely enhanced OER activity and robust stability in alkaline solution (overpotential at 10 mA cm^{-2}: 270 mV; Tafel plots: 64 mV dec^{-1}). Both experimental evidence and density functional theory calculations reveal that the outstanding OER performance of this hybrid catalyst can be attributed to the synergetic effect of exposed cobalt atoms and carbon defects (electron transfer from $CoSe_2$ layer to defect sites at DG). Our results suggest a promising way for the development of highly efficient and low-cost OER catalysts based on transition metal dichalcogenides.

INTRODUCTION

The oxygen evolution reaction (OER) plays an important role in various energy storage technologies, such as H_2 production from water splitting and rechargeable metal-air batteries (Hunter et al., 2016; Suen et al., 2017; Xia et al., 2016; Xu et al., 2016). However, the inherent sluggish OER kinetics, involving a four-electron transfer associated with O-H bond breaking and O-O bond formation, significantly inhibits the large-scale electrochemical water splitting (Dau et al., 2010; Suntivich et al., 2011). Although precious metal oxides (such as RuO_2 and IrO_2) have currently been employed as the state-of-the-art catalysts to overcome the drawback of very low OER kinetics, the high cost and limited resources seriously impede their widespread application (Li and Dai, 2014). As a consequence, it is crucial to explore highly efficient and inexpensive alternative catalysts that are made of geologically abundant elements.

Recently, many economical cobalt-based catalysts, including metal oxides (Masa et al., 2014), phosphates (Zhou et al., 2016), perovskite (Fabbri et al., 2015), hydro(oxy)oxides (Wan et al., 2017), and chalcogenides (Hao et al., 2017; Gao et al., 2017) have been developed and exhibited remarkable OER performance. Notably, $CoSe_2$, with a $t_{2g}^6e_g^1$ electronic configuration close to the optimal e_g filling for OER was considered as an ideal candidate (Kong et al., 2014; Gao et al., 2012). However, the originally synthesized pure $CoSe_2$ catalysts still showed unsatisfied OER activity, inferior to that of the corresponding oxides or hydro(oxy)oxides. Thus, with the purpose of optimizing the OER electrocatalytic performance of $CoSe_2$, tremendous efforts have been made to develop diverse strategies: (1) creating strong chemical and electrical coupling by constructing hybrid structures with metals, metal oxides, or carbon materials (Zheng et al., 2015a, 2015b; Gao et al., 2014; Zhao et al., 2017a, 2017b); (2) increasing the number of active sites by reducing the thickness into atomic scale and introducing more defects (Liu et al., 2014; Liang et al., 2015); and (3) rationally engineering the electrical conductivity by doping metal cations or non-metal heteroatoms (Zhao et al., 2017a, 2017b; Fang et al., 2017). The search for new nanocomposites based on $CoSe_2$, which are comparable to nonprecious metal catalysts, continues (Gao et al., 2017). Specifically, modification of pure $CoSe_2$ by increasing its number of active sites or improving its electrical conductivity could not effectively regulate the electronic configuration of cobalt to optimize OER catalytic activity of each active site, which accordingly restrained the overall performance. To solve the problem, hybridizing with other functional materials offered a promising way. It had been demonstrated that electron-deficient cobalt with high valence could facilitate transforming O* to OOH* (key intermediates in OER process) (Wan et al., 2017). Therefore, if foreign materials grafted with $CoSe_2$ can induce electron donation from cobalt to

[1]Division of Nanomaterials & Chemistry, Hefei National Laboratory for Physical Sciences at the Microscale, Collaborative Innovation Center of Suzhou Nano Science and Technology, Department of Chemistry, CAS Centre for Excellence in Nanoscience, Hefei Science Centre of CAS, University of Science and Technology of China, Hefei 230026, China

[2]School of Natural Sciences and Queensland, Micro- and Nanotechnology Centre, Griffith University, Nathan Campus, Brisbane 4111, Australia

[3]School of Chemical Engineering, University of Queensland, Brisbane 4072, Australia

[4]School of Chemistry, Physics and Mechanical Engineering, Queensland University of Technology, Brisbane, QLD 4000, Australia

[5]These authors contributed equally

[6]Lead Contact

*Correspondence: x.yao@griffith.edu.au (X.Y.), shyu@ustc.edu.cn (S.-H.Y.)

https://doi.org/10.1016/j.isci.2018.08.013

the foreigners, the OER performance should be significantly promoted. However, in most previously reported hybrid OER catalysts based on $CoSe_2$, electrons usually transferred from grafting materials to $CoSe_2$ host, contrary to our assumption, thus encouraging us to develop new hybrid material systems for optimal performance gains.

Non-doped graphene with structural defects has recently received growing attention due to its excellent performance in electrocatalysis (Tang et al., 2016; Jia et al., 2016; Liu et al., 2017; Yan et al., 2017). Incorporation of different types of defects into the sp^2 structure of graphene can effectively break the integrity of π conjugation to enhance the electrocatalytic activity (Tang and Zhang, 2017). Besides, the defects on defective graphene (DG) can also offer additional efficient anchor sites for directly coupling other functional metal-based species, such as Mn-Co nanoparticles and Ni-Fe double layered hydroxide (LDH) nanosheets, through strong chemical interaction at two-phase interface (Yan et al., 2016; Jia et al., 2017). These hybrid catalysts can exhibit much better electrochemical performance than individual components due to their unique structural features such as highly exposed active sites on 2D nanolayers, conductive graphene substrates, as well as enhanced proton coupling and electron transport between the components. Particularly, in the case of Ni-Fe LDH nanosheets hybridized with DG, density functional theory (DFT) calculations had confirmed the accumulation of holes on Ni-Fe LDH nanosheets and that of electrons at the defect sites in DG (Jia et al., 2017). In this regard, properly integrating pre-synthesized 2D $CoSe_2$ nanosheets onto DG may be an effective way to modulate the interfaces and chemical and electronic structures to access optimized OER energetics.

Herein, we report that exfoliated ultrathin $CoSe_2$ nanosheets can be grafted with DG to form a $CoSe_2$@DG hybrid OER catalyst by a facile hydrothermal method. Benefiting from the synergistic effect between $CoSe_2$ and DG substrate, the as-prepared $CoSe_2$@DG nanocomposite exhibits a remarkable performance toward OER. The OER overpotential at a current density of 10 mA cm^{-2} is only 270 mV and a high current density of 129 mA cm^{-2} is obtained at an overpotential of 350 mV, which can be ranked as the top-performing one among the hitherto reported $CoSe_2$-based OER catalysts. In addition, the $CoSe_2$@DG electrode also demonstrates an outstanding stability after a long-term cycle measurement. This work demonstrated that the $CoSe_2$@DG will be a very promising nonprecious metal-based OER catalyst.

RESULTS

Synthesis and Characterization of $CoSe_2$@DG Composite Catalysts

As illustrated in Figure 1A, the whole synthesizing process includes two steps: (1) ultrasound induced liquid exfoliation of pre-synthesized lamellar $CoSe_2$/DETA (diethylenetriamine) intermediate (Liu et al., 2014) and (2) assembling ultrathin $CoSe_2$ nanosheets with DG via a simple hydrothermal route. For the first step, a homogeneously dispersed black suspension was obtained after the ultrasonic exfoliation process, which could keep stable for a long time without any precipitate (Figure 1A, inset). Morphology characterization (scanning electron micrographs and transmission electron microscopic [TEM] images in Figures S1 and S2) clearly confirmed the formation of ultrathin $CoSe_2$ nanosheets (denoted as E-$CoSe_2$). X-ray diffraction (XRD) patterns showed weaker characteristic peaks when compared with pristine $CoSe_2$/DETA, which further demonstrated the well-done exfoliation (Figure 1G, red). The thickness of the exfoliated nanosheets was measured to be around 3 nm from the atomic force microscopic image, corresponding to about 5 layers (a single $CoSe_2$ layer along the lattice parameter is ~0.61 nm) (Figure 1B) (Gao et al., 2009). Subsequently, these $CoSe_2$ ultrathin sheets could be tightly overlain on the DG in a certain mass ratio (typically 9:1) by a hydrothermal treatment process at 60°C for 24 hr. TEM images revealed that the smooth and near-transparent surface of DG sheets became extremely rougher and opaque, indicating the successful grafting of $CoSe_2$ onto DG (Figures 1C and 1D). The high-resolution TEM image in Figure 1E showed the lattice fringe with a spacing of 2.67 Å, which can be assigned to the (210) plane of cubic-phase $CoSe_2$. The interlayer distance could be estimated to be ~5.5 Å, smaller than that of pristine $CoSe_2$/DETA, which was attributed to the removal of DETA molecules during the exfoliation process (Figure 1F). Further experiments revealed that the mass ratio of $CoSe_2$/DG showed a considerable influence on the morphology of the products (Figure S3). When decreasing the mass ratio to 3:1 or 6:1, only partially and non-uniformly covered $CoSe_2$@DG hybrids could be obtained. In addition, DG support also plays an important role in the synthesis. To demonstrate it, $CoSe_2$@G (G presents pristine graphene) and $CoSe_2$@NG (NG represents nitrogen-doped G) samples were fabricated for comparison using the same method. As illustrated in the TEM images, aggregated $CoSe_2$ only anchored on part of G or NG sheet surface, in contrast to the entirely covered morphology for $CoSe_2$@DG (Figure S4). This indicates that DG is more suitable as the support for $CoSe_2$ nanosheet

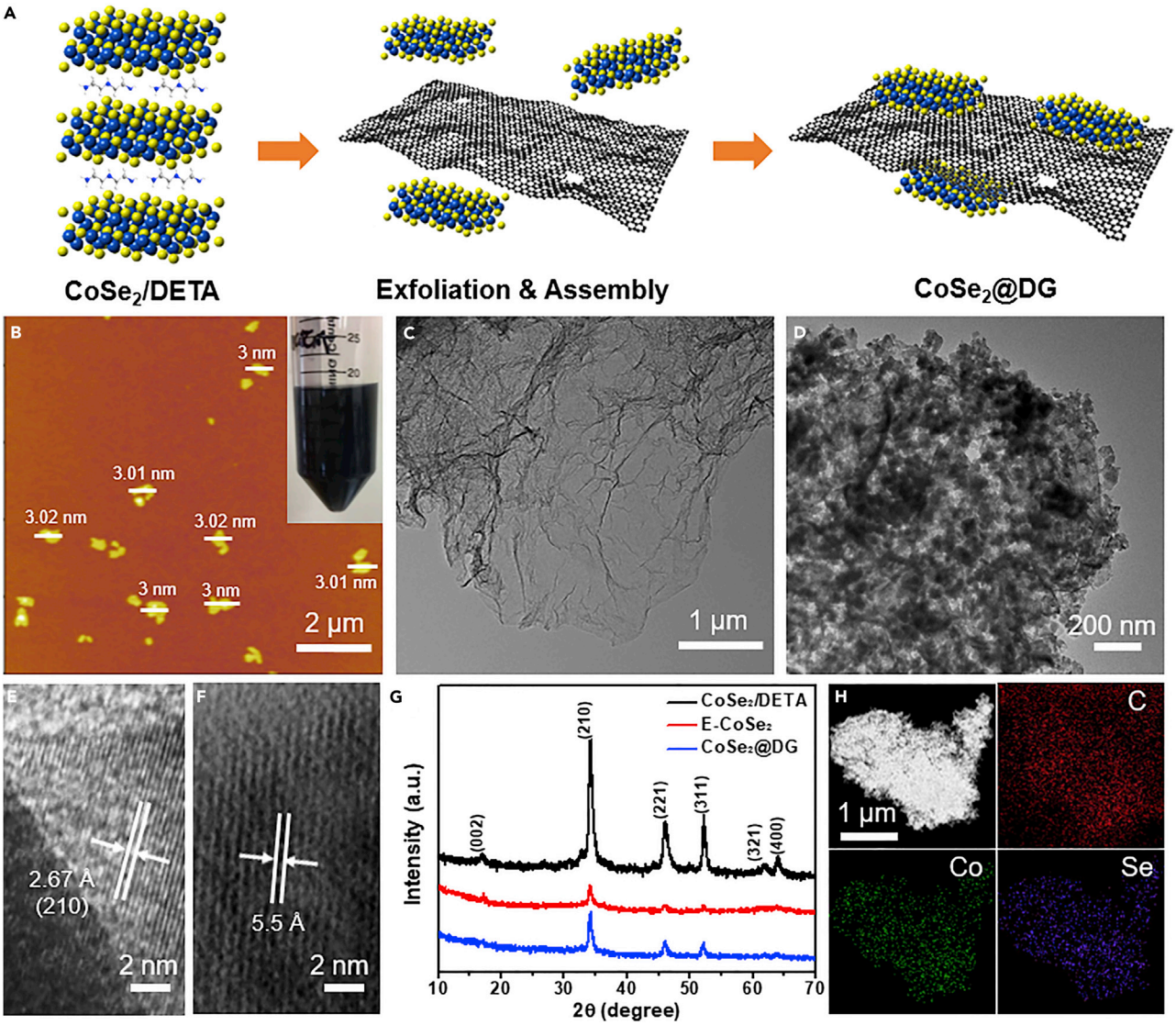

Figure 1. Schematic Illustration of the Synthesis and Characterization of As-prepared $CoSe_2$@DG Composites

(A) Schematic illustration of the fabrication of $CoSe_2$@DG composites.

(B) AFM image of exfoliated $CoSe_2$ nanosheets. Inset: homogeneously dispersed exfoliated $CoSe_2$ nanosheets suspension.

(C and D) TEM images of pristine DG (C) and $CoSe_2$@DG composites (D).

(E and F) High-resolution TEM images of $CoSe_2$@DG composites.

(G) XRD patterns of $CoSe_2$/DETA lamellar intermediates, exfoliated $CoSe_2$ nanosheets, and $CoSe_2$@DG composites.

(H) Scanning transmission electron microscope (STEM)-energy-dispersive X-ray spectrum elemental mapping images of $CoSe_2$@DG composites.

dispersion and anchoring, effectively preventing the aggregation of $CoSe_2$ nanosheets, which should be beneficial for the catalytic performance enhancement.

To further investigate the microstructure and composition of as-prepared $CoSe_2$@DG composites, a series of measurements were carried out. XRD pattern of $CoSe_2$@DG nanocomposites still exhibited the featured diffraction peaks of $CoSe_2$, suggesting that no phase change occurred during the synthesis process (Figure 1G, blue). The intensity of all the peaks was a bit stronger than that of exfoliated ultrathin $CoSe_2$ nanosheets, but still much weaker than that of original $CoSe_2$/DETA, indicating only a small part of ultrathin nanosheets reassembled. In addition, the energy-dispersive X-ray spectrum and elemental mapping indicated the existence of elements C, Co, Se and their uniform distribution in the hybrids, also confirming the formation of $CoSe_2$@DG composites (Figures 1H and S5). The Co loading amount in as-made $CoSe_2$@DG,

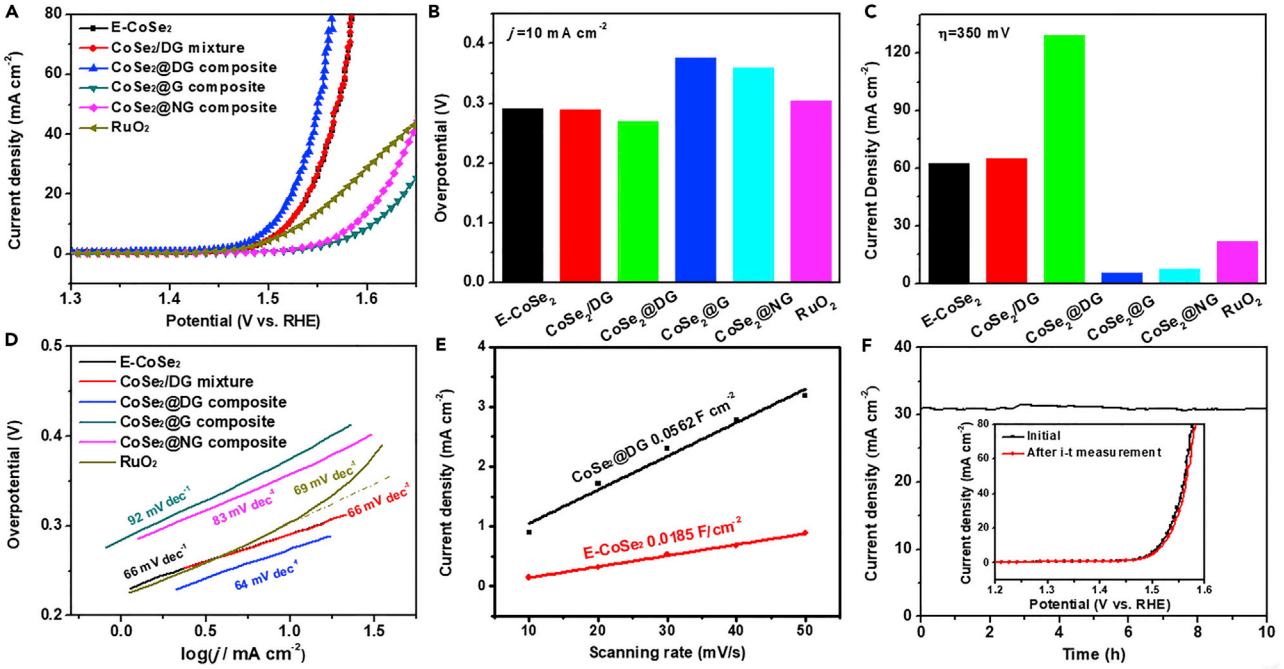

Figure 2. OER Performance of $CoSe_2$@DG Composite Catalysts

(A) OER LSV curves of different catalysts in O_2-saturated 1 M KOH solution.

(B) Overpotential required for j = 10 mA cm^{-2}.

(C) Current densities at an overpotential of 350 mV.

(D) The corresponding Tafel plots.

(E) Scan rate dependence of the current density difference for exfoliated $CoSe_2$ nanosheets and $CoSe_2$@DG composites. The linear slope is equivalent to twice the double-layer capacitance C_{dl}.

(F) Continuous amperometric i-t measurement at a constant overpotential of 305 mV. The inset shows the polarization curves before and after i-t measurement.

$CoSe_2$@G, and $CoSe_2$@NG composites was obtained according to the thermogravimetric analysis as 31.6, 28.9, 29.5 wt%, respectively (Figure S6). Based on this, we further calculated the number of moles (n) of Co element in different catalysts deposited on the glass carbon electrode ($CoSe_2$@DG: 0.132 μmol; $CoSe_2$@G: 0.121 μmol; $CoSe_2$@NG: 0.124 μmol), which could be used to gain the turnover frequency (TOF) value for the evaluation of their intrinsic OER efficiency.

OER Performance of $CoSe_2$@DG Catalysts-Coated Glass Carbon Electrode

Using a standard three-electrode system, the electrocatalytic OER properties of different samples were evaluated in an O_2-saturated 1 M KOH aqueous solution ($4OH^- \rightarrow O_2 + 2H_2O + 4e^-$). The as-prepared catalysts were uniformly cast on a glassy carbon electrode with a loading of 0.2 mg cm^{-2} and used as a working electrode. The OER activities of $CoSe_2$@DG composites prepared with different mass ratios (3:1, 6:1, and 9:1) were first studied to determine the optimal synthetic condition. As shown in Figure S7, $CoSe_2$@DG-9-1 exhibited the best OER activity among the three products, with the smallest overpotential at 10 mA cm^{-2}, the largest current density at an overpotential of 0.35 V, and the fastest kinetics. The results should be attributed to their morphological difference mentioned above. Reassembly of $CoSe_2$ nanosheets in $CoSe_2$@DG-3-1 and $CoSe_2$@DG-6-1 samples significantly inhibited their OER performance. If not specially specified, the $CoSe_2$@DG, $CoSe_2$@NG, and $CoSe_2$@G products are all synthesized in the mass ratio of 9:1 in this research. Subsequently, the OER activities for other comparative samples, such as $CoSe_2$ nanosheets coupling with different graphene (NG, G), exfoliated $CoSe_2$ nanosheet (E-$CoSe_2$), $CoSe_2$ nanosheets physically mixed with DG ($CoSe_2$/DG), and the OER benchmark catalyst (RuO_2), were also measured. Figure 2A shows polarization curves recorded by linear sweep voltammetry (LSV) at a slow scan rate of 5 mV s^{-1} with a continuous rotating speed of 1,600 rpm after internal resistance (iR) correction. Among the five tested catalysts, $CoSe_2$@DG displayed the highest intrinsic OER activity. To reach a current density of 10 mA cm^{-2}, $CoSe_2$@DG required an overpotential of only 270 mV, which was 35, 22, 20, 106, and 83 mV smaller than that

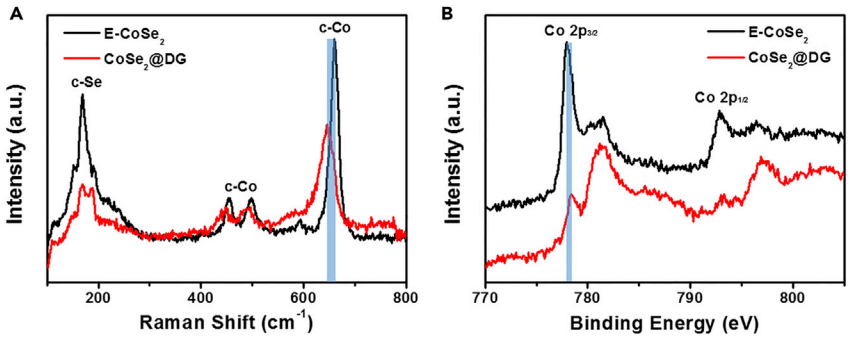

Figure 3. Study of Interaction between $CoSe_2$ and DG in the Composite Catalysts

(A and B) Raman spectra (A) and high-resolution Co 2p XPS (B) of exfoliated $CoSe_2$ nanosheets and $CoSe_2$@DG composites.

of commercial RuO_2, E-$CoSe_2$, $CoSe_2$/DG mixture, $CoSe_2$@G, and $CoSe_2$@NG, respectively (Figure 2B). The current density at an overpotential of 350 mV was 129 mA cm^{-2}, which was 6, 2.1, 2, 23.7, and 16.5 times higher than that of RuO_2, E-$CoSe_2$, $CoSe_2$/DG mixture, $CoSe_2$@G, and $CoSe_2$@NG, respectively (Figure 2C). Meanwhile, the intrinsic activity of different catalysts was assessed by TOF, assuming all the Co element was catalytically active (Figure S8). Compared with RuO_2, E-$CoSe_2$, $CoSe_2$@G, and $CoSe_2$@NG catalysts, the $CoSe_2$@DG hybrids exhibited obviously larger TOF value of 0.024 s^{-1} at an overpotential of 270 mV, indicating the significant role of interaction between $CoSe_2$ and DG toward OER in our study. As all the active sites were presumed to come from $CoSe_2$, comparative experiment was also offered to confirm that DG was inert in OER relative to $CoSe_2$ (Figure S9). Furthermore, the kinetic parameters of OER for the five catalysts were also calculated (Figure 2D). $CoSe_2$@DG had a Tafel slope of about 64 mV dec^{-1}, similar to that of E-$CoSe_2$ (66 mV dec^{-1}), $CoSe_2$/DG mixture (66 mV dec^{-1}), and RuO_2 (69 mV dec^{-1}), but much smaller than that of the other samples (83 mV dec^{-1} for $CoSe_2$@NG and 92 mV dec^{-1} for $CoSe_2$@G). The above OER measurement was done in 1 M KOH solution. However, in some cases, OER catalysts were reported to assess their activity in 0.1 M KOH solution (Liu et al., 2014). Therefore, to achieve a more accurate comparison of the OER performance between our synthesized $CoSe_2$@DG hybrid catalyst and other nonprecious metal catalysts, we also measured its OER LSV curves in 0.1 M KOH solution and found that it only required an overpotential of 304 mV to afford a current density of 10 mA cm^{-2} (Figure S10). In fact, the activity of $CoSe_2$@DG has outperformed those of most $CoSe_2$-based OER catalysts reported to date and is comparable to those of other state-of-the-art nonprecious metal catalysts (Table S1). To gain further insight of the OER kinetics occurring on such $CoSe_2$@DG hybrid catalysts, electrical impedance spectroscopy was performed. The $CoSe_2$@DG composites exhibited a much smaller charge transfer resistance of 42 Ω than that of E-$CoSe_2$ of 88 Ω (Figure S11). Moreover, the double layer capacitance (C_{dl}) was obtained through the cyclic voltammetry measurement, which was considered as an alternative method to estimate the electrochemical active surface areas (ECSAs) (Figures 2E and S12). The $CoSe_2$@DG composites show a C_{dl} of 28.1 mF cm^{-2}, much larger than that of E-$CoSe_2$ nanosheets (9.3 mF cm^{-2}), indicating that the effective combination of $CoSe_2$ and DG leads to an increased ECSA and more exposed active sites.

To assess the stability of the conditioned $CoSe_2$@DG electrode, the continuous amperometric i-t measurement was employed under a constant overpotential of 305 mV. Figure 2F displayed that the current density maintained at ~ 31 mA cm^{-2} during 10 hr and the polarization curve after i-t measurement showed negligible current loss, demonstrating the high electrocatalytic durability of $CoSe_2$@DG. Various postmortem characterizations reveal no obvious change in the structure of $CoSe_2$@DG catalysts after OER stability test, further evidencing their remarkable catalytic robustness in alkaline medium (Figure S13).

Catalytic Mechanism by Synergistic Effect of $CoSe_2$ with DG

It is imperative to gain a comprehensive understanding of the intrinsic reason for the improved OER performance after the effective coupling of $CoSe_2$ and DG. To achieve this goal, both experimental and theoretical methods were used. First, the strong interactions between $CoSe_2$ and DG in the composites were demonstrated experimentally by Raman scattering and X-ray photoelectron spectroscopic (XPS) measurements, indicating that the synthetic effect should play a vital role for OER enhancement (Figure 3).

As shown in Figure 3A, both E-$CoSe_2$ and $CoSe_2$@DG samples exhibited four characteristic peaks corresponding to the cubic $CoSe_2$ (Campos et al., 2002). Notably, the Raman peak at ~660 cm^{-1} shifted to lower wave number after incorporating $CoSe_2$ with DG, suggesting the charge transfer between $CoSe_2$ nanosheets and DG substrates, which resembled previous observation in the case of $CeO_2/CoSe_2$ and Au cluster/$CoSe_2$ composites (Zheng et al., 2015a, 2015b; Zhao et al., 2017a, 2017b). In addition, we also compared the Raman spectra of DG and $CoSe_2$@DG and found that the characteristic D band (1,344 cm^{-1}) and G band (1,574 cm^{-1}) became much weaker after anchoring $CoSe_2$ on DG (Figure S14) (Banhart et al., 2011). This change can be ascribed to the relatively low amount of DG in the $CoSe_2$@DG composite (prepared in the mass ratio of 9:1 for $CoSe_2$ and DG as depicted above). To further confirm the interaction between $CoSe_2$ layer and defects on DG, XPS of E-$CoSe_2$ and $CoSe_2$@DG were carried out. The Co^{3+} cations were generally believed to be the real reason for the decent OER activity, which could facilitate the formation of O—OH (key intermediates in OER) and then further be oxidized to produce O_2 (Chen et al., 2016; Yeo and Bell, 2011). As shown in the high-resolution Co 2p spectra, there existed obvious characteristic peaks of Co^{2+} and Co^{3+} cations, which was in accordance with that of $CoSe_2$ materials reported previously (Figure 3B) (Li et al., 2017). Of note, the electron binding energy of Co 2p in $CoSe_2$@DG composites showed an ~0.4 eV increase compared with pure E-$CoSe_2$, which indicated the effective electron transfer from $CoSe_2$ to DG (Gao et al., 2012; Zheng et al., 2015a, 2015b). Both Raman spectra and XPS results demonstrated that the synergetic effect between $CoSe_2$ and DG could change the electron configuration in the composites, which consequently promoted their OER performance. Moreover, perhaps someone will wonder whether the hydrothermal process has positive influence on the $CoSe_2$ nanosheets for the improved OER activity of final $CoSe_2$@DG composites. To exclude it, hydrothermal-treated $CoSe_2$ (H-$CoSe_2$) without DG was also prepared (Figure S15). LSV curves illustrated that H-$CoSe_2$ showed decreased OER activity than original E-$CoSe_2$, further proving that the synergetic effect of $CoSe_2$ and DG was the cause of the enhanced OER performance for $CoSe_2$@DG composites.

Based on above experimental data, we have attributed the enhanced OER activity after coupling $CoSe_2$ nanosheets and DG to the effective charge transfer from $CoSe_2$ layer to DG. To further demonstrate it, we conducted a series of DFT calculations (see computational details in the Supplemental Information). In a previous study, we have confirmed that different defect types (denoted as DG-5, DG-585, and DG-5775 defect) on DG serve as highly efficient catalytically active sites (Jia et al., 2016). Therefore, we chose the three defect types as the computational models of DG in this part. Figures 4A–4C and S16 showed the geometries of the fully relaxed $CoSe_2$@DG-5, $CoSe_2$@DG-585, $CoSe_2$@DG-5775, $CoSe_2$@NG, and $CoSe_2$@G composites in side view and their charge density differences. It could be seen clearly that the electrons were inclined to redistribute around the 5 and 585 defect sites, resulting in the charge depletion on $CoSe_2$ layer, which favors OER (Figure 4D). In contrast, the electron transfer in the other three models was negligible. The calculation results on the charge transfer between the two components were consistent with our experimental data. Moreover, we also calculated the Gibbs free energy differences for OER occurring on $CoSe_2$@DG, $CoSe_2$@NG, $CoSe_2$@G composites, and pristine $CoSe_2$ (Figure 4E). The ideal barrier (1.23 eV) for each step was also included for comparison (black thick line). The overpotential was determined by the largest Gibbs free energy barrier. For the pristine $CoSe_2$, $CoSe_2$@G, $CoSe_2$@DG, and $CoSe_2$@NG composites, the third step (O* is transformed to OOH*) is the rate-determining step. As observed, the $CoSe_2$@DG composite possessed the lowest Gibbs free energy with a barrier of 1.39 eV among the models, indicating its best OER activity. Both experimental and theoretical results demonstrate that the charge depletion on $CoSe_2$ induced by the electron transfer from $CoSe_2$ to DG is the cause of the outstanding OER performance of the $CoSe_2$@DG catalysts.

DISCUSSION

In summary, we have successfully grafted exfoliated $CoSe_2$ nanosheets onto the DG to prepare a new $CoSe_2$@DG composite by a hydrothermal process. The hybrid catalyst displays excellent OER performance with a small overpotential of ~270 mV at a current density of 10 mA cm^{-2}, large anodic current density of ~129 mA cm^{-2} at an overpotential of 350 mV, and good durability in alkaline solution, which is superior to most reported $CoSe_2$-based OER catalysts. Based on our experimental analysis and DFT calculations, the improved OER activity can be attributed to the synergistic effect (charge redistribution) between $CoSe_2$ nanosheets and DG substrates. This work will raise promising possibilities for designing advanced OER electrocatalysts via synergistically coupling nonprecious metal-based materials with DG, which is highly desirable for energy conversion technologies.

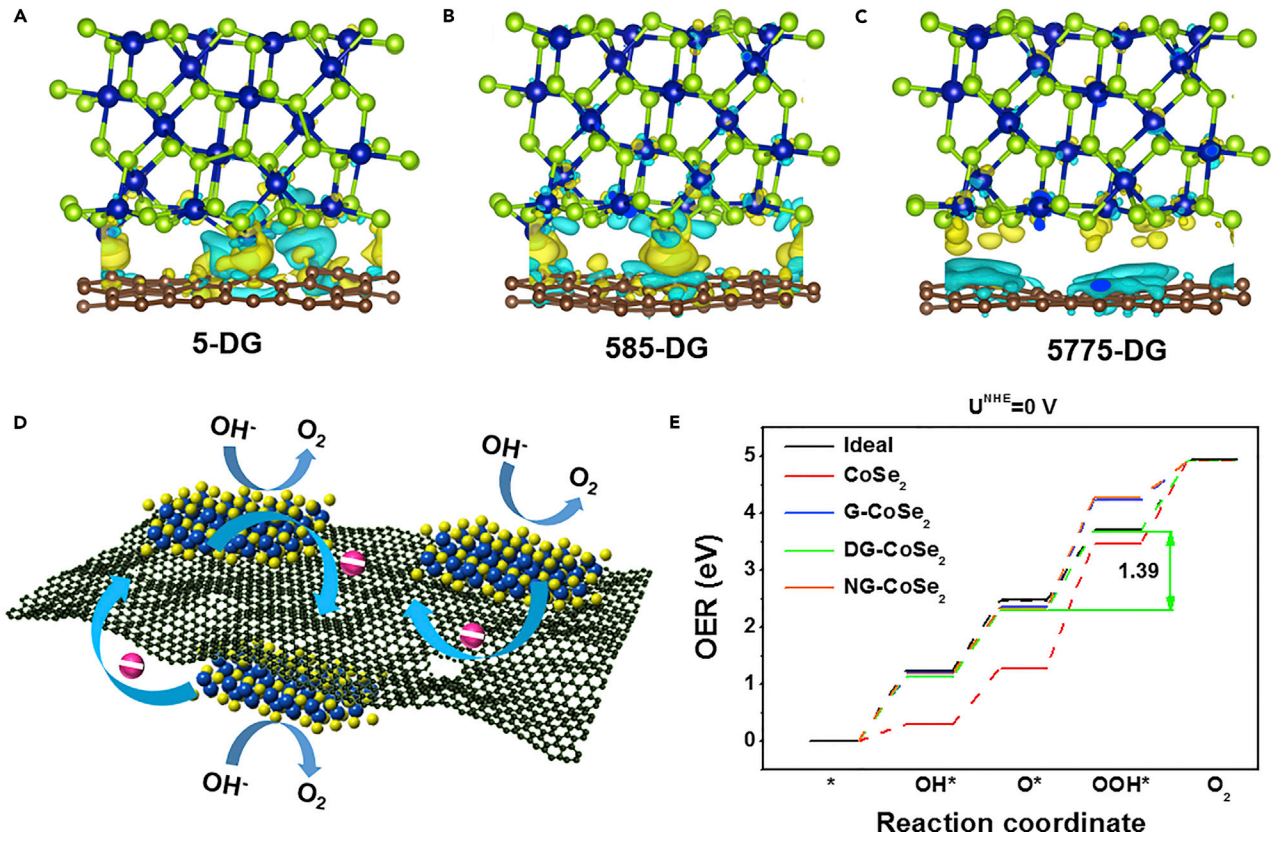

Figure 4. Understanding of OER Catalytic Mechanism on $CoSe_2$@DG Catalysts

(A–C) The side views of 3D charge density difference plot for the interfaces between a defective graphene sheet [DG-5 (A), DG-585 (B), DG-5775 (C)] and $CoSe_2$ layer are calculated by DFT. Yellow and cyan isosurfaces represent charge accumulation and depletion in the 3D space with an isosurface value of 0.002 e $Å^{-3}$. Brown, green, and blue balls represent C, Se, and Co atoms, respectively.

(D) The schematic of the probable OER mechanism of $CoSe_2$@DG composites is presented based on the DFT calculation results. The pink spheres represent electrons.

(E) The free energy diagram for oxygen evolution on pristine $CoSe_2$, $CoSe_2$@G, $CoSe_2$@DG, and $CoSe_2$@NG composites. The ideal catalyst with a barrier of 1.23 eV for each step is also included for comparison (black thick line).

Limitations of Study

This work proposes a promising avenue to enhance catalytic performance by effective hybridization of carbon defects and foreign materials. Although demonstrated theoretically, the fabrication of a certain type of carbon defect is now experimentally unavailable, limiting the further optimization of catalytic energetics for such composite catalysts.

METHODS

All methods can be found in the accompanying Transparent Methods supplemental file.

SUPPLEMENTAL INFORMATION

Supplemental Information includes Transparent Methods, 16 figures, and 1 table and can be found with this article online at https://doi.org/10.1016/j.isci.2018.08.013.

ACKNOWLEDGMENTS

The authors appreciate the funding support from the National Natural Science Foundation of China (Grants 51732011, 21431006), the Foundation for Innovative Research Groups of the National Natural Science Foundation of China (Grant 21521001), Key Research Program of Frontier Sciences, CAS (Grant QYZDJSSW-SLH036), the National Basic Research Program of China (Grant 2014CB931800), the Users

with Excellence and Scientific Research Grant of Hefei Science Center of CAS (2015HSC-UE007, 2015SRG-HSC038), the Australian Research Council (ARC DP170103317), the China Postdoctoral Science Foundation (Grant BH2060000037), and the Fundamental Research Funds for the Central Universities (Grant WK2060190057), the authors also would like to thank the Australian National Fabrication Facility (ANFF-Q) for the AFM test.

AUTHOR CONTRIBUTIONS

X.W. and L.Zhuang contributed equally to this work. X.W., L.Zhuang, X.Yao, and S.Y. conceived and designed the experiments. M.G., Z.Z., X.Yao, and S.H.Y. supervised the project. X.W., L.Zhuang, Y.J., L.Zhang, and X.Yan performed the synthesis experiments, material characterization, and OER measurement. T.H. and A.D. performed the DFT calculation. All authors discussed the results and commented on the manuscript.

DECLARATION OF INTERESTS

The authors declare no competing interests.

Received: April 25, 2018
Revised: July 18, 2018
Accepted: August 10, 2018
Published: September 28, 2018

REFERENCES

Banhart, F., Kotakoski, J., and Krasheninnikov, A.V. (2011). Structural defects in graphene. ACS Nano *5*, 26–41.

Campos, C.E.M., de Lima, J.C., Grandi, T.A., Machado, K.D., and Pizani, P.S. (2002). Structural studies of cobalt selenides prepared by mechanical alloying. Physica B *324*, 409–418.

Chen, W., Liu, Y.Y., Li, Y.Z., Sun, J., Qiu, Y.C., Liu, C., Zhou, G.M., and Cui, Y. (2016). In situ electrochemically derived nanoporous oxides from transition metal dichalcogenides for active oxygen evolution catalysts. Nano Lett. *16*, 7588–7596.

Dau, H., Limberg, C., Reier, T., Risch, M., Roggan, S., and Strasser, P. (2010). The mechanism of water oxidation: from electrolysis via homogeneous to biological catalysis. ChemCatChem *2*, 724–761.

Fabbri, E., Nachtegaal, M., Cheng, X., and Schmidt, T.J. (2015). Superior bifunctional electrocatalytic activity of $Ba_{0.5}Sr_{0.5}Co_{0.8}Fe_{0.2}O_{3-\delta}$/Carbon composite electrodes: insight into the local electronic structure. Adv. Energy Mater. *5*, 1402033.

Fang, L., Li, W., Guan, Y., Feng, Y., Zhang, H., Wang, S., and Wang, Y. (2017). Tuning unique peapod-like $Co(S_xSe_{1-x})_2$ nanoparticles for efficient overall water splitting. Adv. Funct. Mater. https://doi.org/10.1002/adfm.201701008.

Gao, M.-R., Yao, W.-T., Yao, H.-B., and Yu, S.-H. (2009). Synthesis of unique ultrathin lamellar mesostructured $CoSe_2$—amine (protonated) nanobelts in a binary solution. J. Am. Chem. Soc. *131*, 7486–7487.

Gao, M.-R., Xu, Y.-F., Jiang, J., Zheng, Y.-R., and Yu, S.-H. (2012). Water oxidation electrocatalyzed by an efficient $Mn_3O_4/CoSe_2$ nanocomposite. J. Am. Chem. Soc. *134*, 2930–2933.

Gao, M.-R., Cao, X., Gao, Q., Xu, Y.-F., Zheng, Y.-R., Jiang, J., and Yu, S.-H. (2014). Nitrogen-doped graphene supported $CoSe_2$ nanobelt composite catalyst for efficient water oxidation. ACS Nano *8*, 3970–3978.

Gao, M.-R., Zheng, Y.-R., Jiang, J., and Yu, S.-H. (2017). Pyrite-type nanomaterials for advanced electrocatalysis. Acc. Chem. Res. *50*, 2194–2204.

Hao, J., Yang, W., Peng, Z., Zhang, C., Huang, Z., and Shi, W. (2017). A nitrogen doping method for CoS_2 electrocatalysts with enhanced water oxidation performance. ACS Catal. *7*, 4214–4220.

Hunter, B.M., Gray, H.B., and Müller, A.M. (2016). Earth-abundant heterogeneous water oxidation catalysts. Chem. Rev. *116*, 14120–14136.

Jia, Y., Zhang, L., Du, A., Gao, G., Chen, J., Yan, X., Brown, C.L., and Yao, X. (2016). Defect graphene as a trifunctional catalyst for electrochemical reactions. Adv. Mater. *28*, 9532–9538.

Jia, Y., Zhang, L., Gao, G., Chen, H., Wang, B., Zhou, J., Soo, M.T., Hong, M., Yan, X., Qian, G., et al. (2017). A heterostructure coupling of exfoliated Ni–Fe hydroxide nanosheet and defective graphene as a bifunctional electrocatalyst for overall water splitting. Adv. Mater. https://doi.org/10.1002/adma.201700017.

Kong, D., Wang, H., Lu, Z., and Cui, Y. (2014). $CoSe_2$ nanoparticles grown on carbon fiber paper: an efficient and stable electrocatalyst for hydrogen evolution reaction. J. Am. Chem. Soc. *136*, 4897–4900.

Li, Y., and Dai, H. (2014). Recent advances in zinc-air batteries. Chem. Soc. Rev. *43*, 5257–5275.

Li, W., Gao, X., Xiong, D., Wei, F., Song, W.-G., Xu, J., and Liu, L. (2017). Hydrothermal synthesis of monolithic Co_3Se_4 nanowire electrodes for oxygen evolution and overall water splitting with high efficiency and extraordinary catalytic stability. Adv. Energy Mater. https://doi.org/10.1002/aenm.201602579.

Liang, L., Cheng, H., Lei, F., Han, J., Gao, S., Wang, C., Sun, Y., Qamar, S., Wei, S., and Xie, Y. (2015). Metallic single-unit-cell orthorhombic cobalt diselenide atomic layers: robust water-electrolysis catalysts. Angew. Chem. Int. Ed. *54*, 12004–12008.

Liu, Y., Cheng, H., Lyu, M., Fan, S., Liu, Q., Zhang, W., Zhi, Y., Wang, C., Xiao, C., Wei, S., et al. (2014). Low overpotential in vacancy-rich ultrathin $CoSe_2$ nanosheets for water oxidation. J. Am. Chem. Soc. *136*, 15670–15675.

Liu, Z., Zhao, Z., Wang, Y., Dou, S., Yan, D., Liu, D., Xia, Z., and Wang, S. (2017). In situ exfoliated, edge-rich, oxygen-functionalized graphene from carbon fibers for oxygen electrocatalysis. Adv. Mater. https://doi.org/10.1002/adma.201606207.

Masa, J., Xia, W., Sinev, I., Zhao, A., Sun, Z., Grützke, S., Weide, P., Muhler, M., and Schuhmann, W. (2014). Mn_xO_y/NC and Co_xO_y/NC nanoparticles embedded in a nitrogen-doped carbon matrix for high-performance bifunctional oxygen electrodes. Angew. Chem. Int. Ed. *53*, 8508–8512.

Suen, N.-T., Hung, S.-F., Quan, Q., Zhang, N., Xu, Y.-J., and Chen, H.M. (2017). Electrocatalysis for the oxygen evolution reaction: recent development and future perspectives. Chem. Soc. Rev. *46*, 337–365.

Suntivich, J., May, K.J., Gasteiger, H.A., Goodenough, J.B., and Shao-Horn, Y. (2011). A perovskite oxide optimized for oxygen evolution catalysis from molecular orbital principles. Science *334*, 1383–1385.

Tang, C., and Zhang, Q. (2017). Nanocarbon for oxygen reduction electrocatalysis: dopants,

edges, and defects. Adv. Mater. https://doi.org/10.1002/adma.201604103.

Tang, C., Wang, H.-F., Chen, X., Li, B.-Q., Hou, T.-Z., Zhang, B., Zhang, Q., Titirici, M.-M., and Wei, F. (2016). Topological defects in metal-free nanocarbon for oxygen electrocatalysis. Adv. Mater. *28*, 6845–6851.

Wan, S., Qi, J., Zhang, W., Wang, W., Zhang, S., Liu, K., Zheng, H., Sun, J., Wang, S., and Cao, R. (2017). Hierarchical Co(OH)F superstructure built by low-dimensional substructures for electrocatalytic water oxidation. Adv. Mater. https://doi.org/10.1002/adma.2017002861700286.

Xia, B.Y., Yan, Y., Li, N., Wu, H.B., Lou, X.W., and Wang, X. (2016). A metal–organic framework-derived bifunctional oxygen electrocatalyst. Nat. Energy *1*, 15006.

Xu, X., Song, F., and Hu, X. (2016). A nickel iron diselenide-derived efficient oxygen-evolution catalyst. Nat. Commun. *7*, 12324.

Yan, X., Jia, Y., Chen, J., Zhu, Z., and Yao, X. (2016). Defective-activated-carbon-supported Mn–Co nanoparticles as a highly efficient electrocatalyst for oxygen reduction. Adv. Mater. *28*, 8771–8778.

Yan, D., Li, Y., Huo, J., Chen, R., Dai, L., and Wang, S. (2017). Defect chemistry of nonprecious-metal electrocatalysts for oxygen reactions. Adv. Mater. https://doi.org/10.1002/adma.201606459.

Yeo, B.S., and Bell, A.T. (2011). Enhanced activity of gold-supported cobalt oxide for the electrochemical evolution of oxygen. J. Am. Chem. Soc. *133*, 5587–5593.

Zhao, S., Jin, R., Abroshan, H., Zeng, C., Zhang, H., House, S.D., Gottlieb, E., Kim, H.J., Yang, J.C., and Jin, R. (2017a). Gold nanoclusters promote electrocatalytic water oxidation at the nanocluster/$CoSe_2$ interface. J. Am. Chem. Soc. *139*, 1077–1080.

Zhao, X., Zhang, H., Yan, Y., Cao, J., Li, X., Zhou, S., Peng, Z., and Zeng, J. (2017b). Engineering the electrical conductivity of lamellar silver-doped cobalt(ii) selenide nanobelts for enhanced oxygen evolution. Angew. Chem. Int. Ed. *56*, 328–332.

Zheng, Y.-R., Gao, M.-R., Gao, Q., Li, H.-H., Xu, J., Wu, Z.-Y., and Yu, S.-H. (2015a). An efficient CeO_2/$CoSe_2$ nanobelt composite for electrochemical water oxidation. Small *11*, 182–188.

Zheng, Y.-R., Gao, M.-R., Yu, Z.-Y., Gao, Q., Gao, H.-L., and Yu, S.-H. (2015b). Cobalt diselenide nanobelts grafted on carbon fiber felt: an efficient and robust 3d cathode for hydrogen production. Chem. Sci. *6*, 4594–4598.

Zhou, T., Du, Y., Yin, S., Tian, X., Yang, H., Wang, X., Liu, B., Zheng, H., Qiao, S., and Xu, R. (2016). Nitrogen-doped cobalt phosphate@nanocarbon hybrids for efficient electrocatalytic oxygen reduction. Energy Environ. Sci. *9*, 2563–2570.

ISCI, Volume 7

Supplemental Information

Grafting Cobalt Diselenide on Defective Graphene for Enhanced Oxygen Evolution Reaction

Xin Wang, Linzhou Zhuang, Tianwei He, Yi Jia, Longzhou Zhang, Xuecheng Yan, Minrui Gao, Aijun Du, Zhonghua Zhu, Xiangdong Yao, and Shu-Hong Yu

Supplemental Information

Supplemental Figures

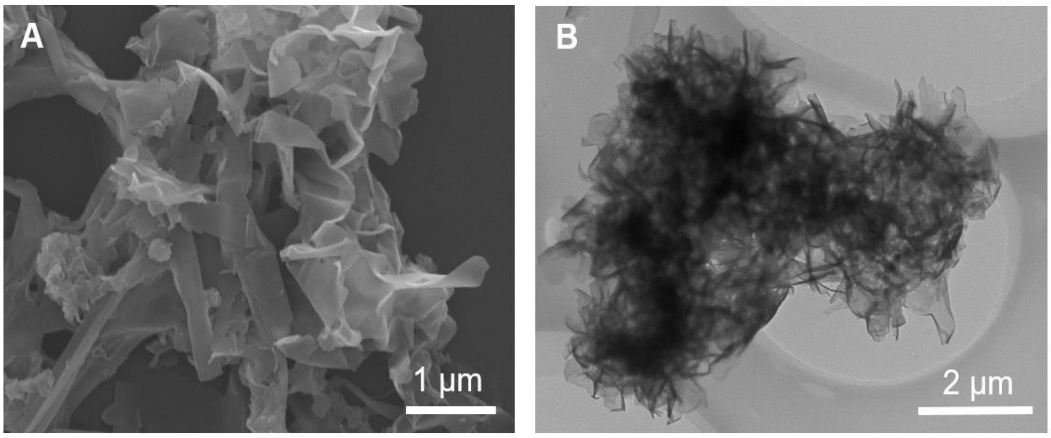

Figure S1. Characterization of $CoSe_2$/DETA hybrids, related to Figure 1.
SEM (A) and TEM (B) images of synthesized $CoSe_2$/DETA hybrids.

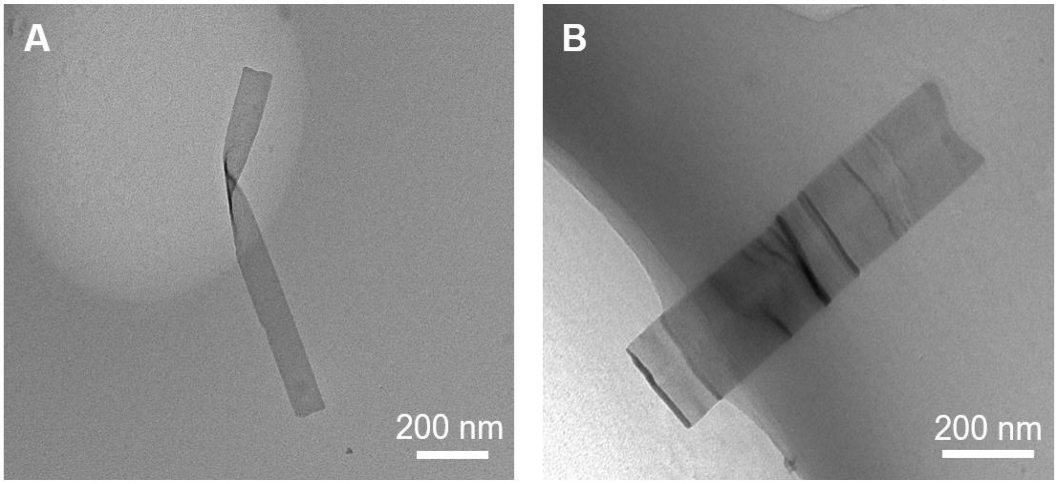

Figure S2. Characterization of exfoliated $CoSe_2$ ultrathin nanosheets, related to Figure 1.
TEM images of exfoliated $CoSe_2$ ultrathin nanosheets.

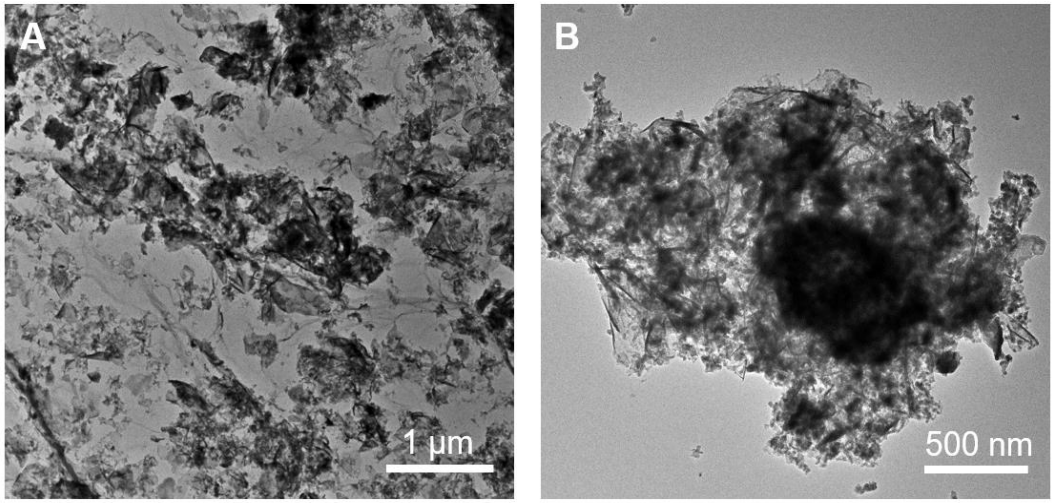

Figure S3. Characterization of different $CoSe_2$@DG samples, related to Figure 1.

TEM images of $CoSe_2$@DG samples prepared with the mass ratio of $CoSe_2$/DG as (A) 3:1 and (B) 6:1.

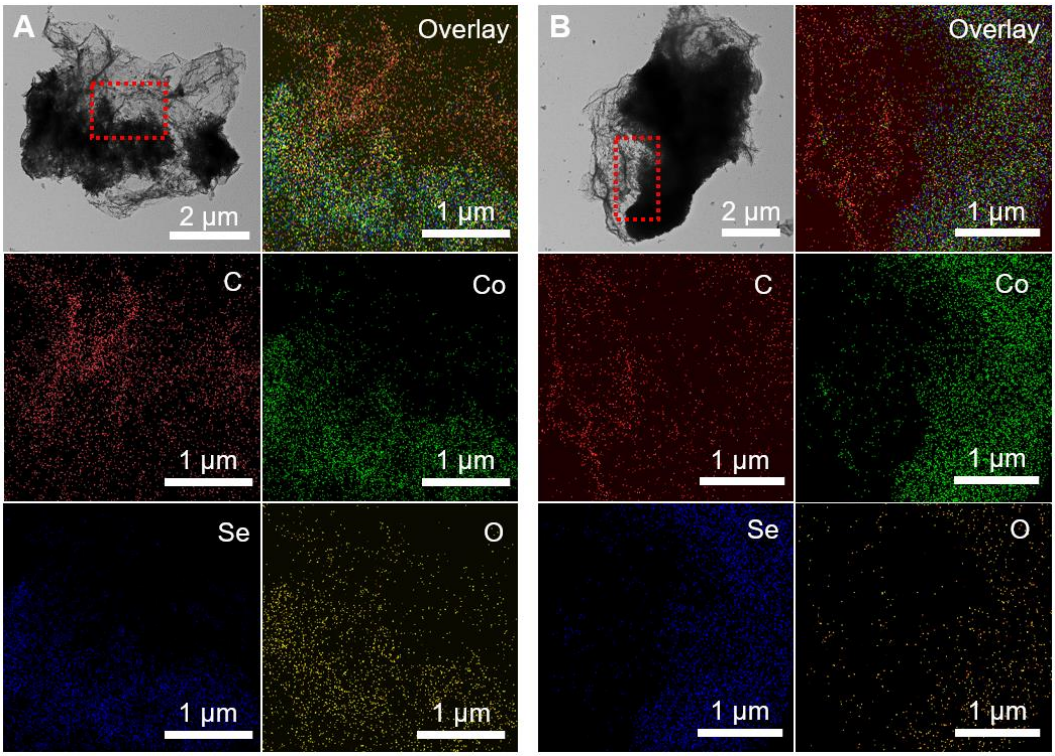

Figure S4. Characterization of $CoSe_2$@G and $CoSe_2$@NG composites, related to Figure 1.

STEM-EDS elemental mapping images of (A) $CoSe_2$@G and (B) $CoSe_2$@NG composites.

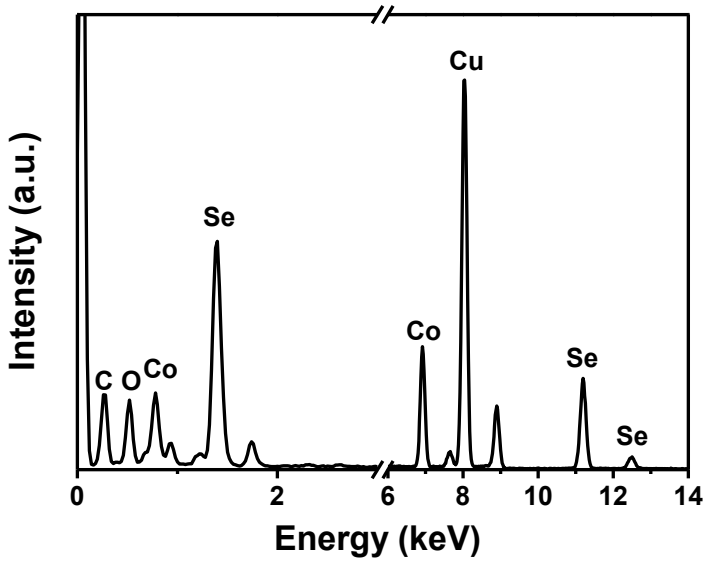

Figure S5. Characterization of $CoSe_2$@DG composites, related to Figure 1.
EDX spectrum of as-prepared $CoSe_2$@DG composites.

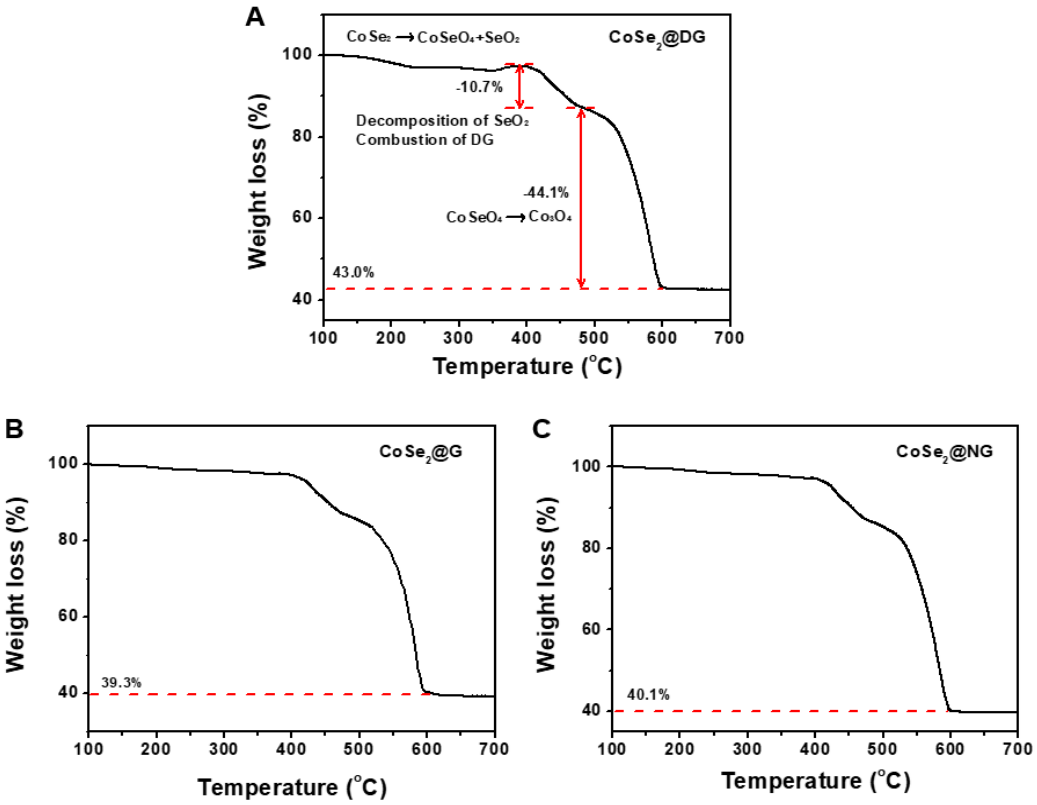

Figure S6. Characterization of $CoSe_2$@G, $CoSe_2$@NG, and $CoSe_2$@DG composites, related to Figure 1.

TGA curve of (A) $CoSe_2$@DG, (B) $CoSe_2$@G, (C) $CoSe_2$@NG composites under air atmosphere.

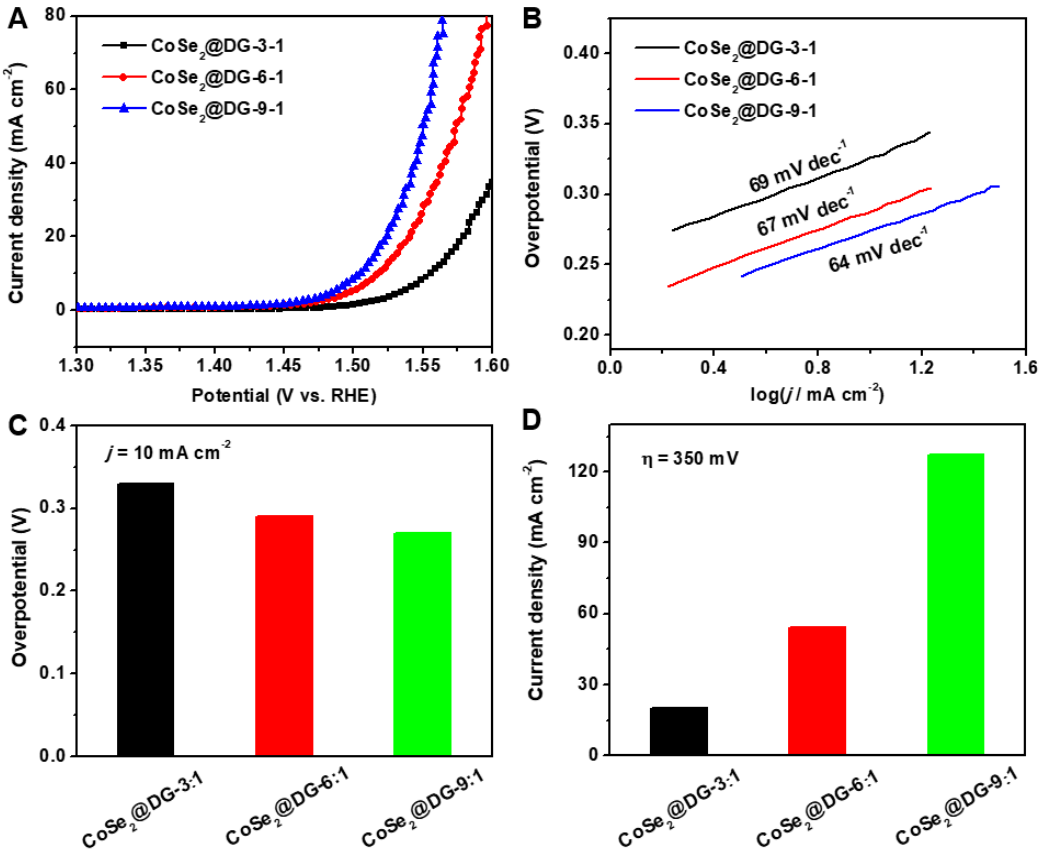

Figure S7. OER activity of $CoSe_2$@DG composites prepared with different mass ratio (3:1, 6:1, and 9:1), related to Figure 2.

(A) LSV curves, (B) Tafel plots, (C) Overpotential required for j=10 mA cm^{-2}, (D) Current densities at an overpotential of 350 mV.

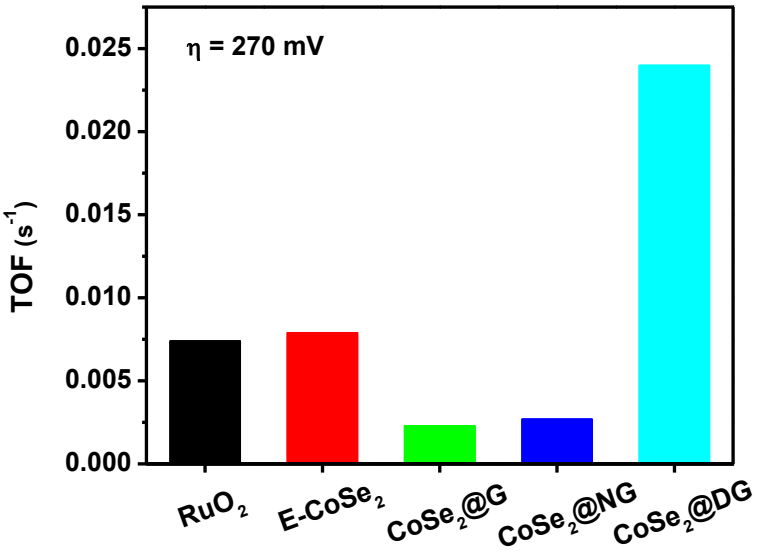

Figure S8. Intrinsic activity study of different catalysts, related to Figure 2.
Turnover frequency (TOF) of different catalysts at an overpotential of 270 mV.

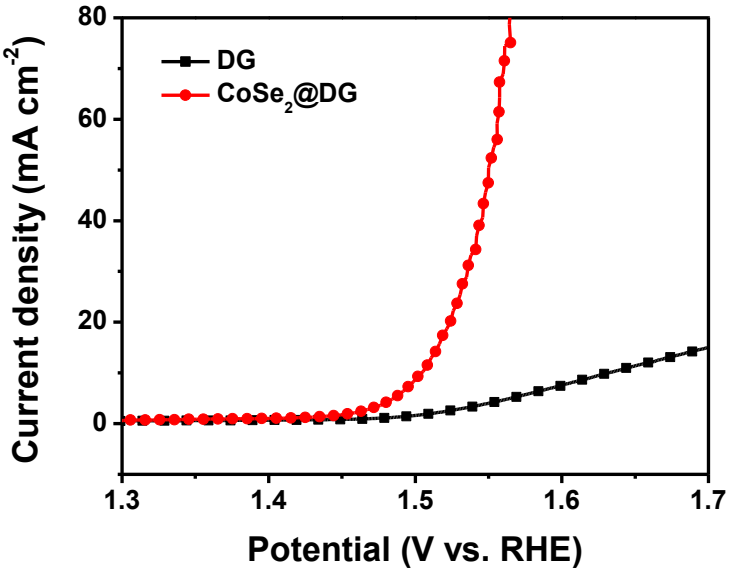

Figure S9. Comparison of OER activity between DG and $CoSe_2$@DG hybrid, related to Figure 2.
OER LSV curves of DG and $CoSe_2$@DG hybrid in 1 M KOH solution

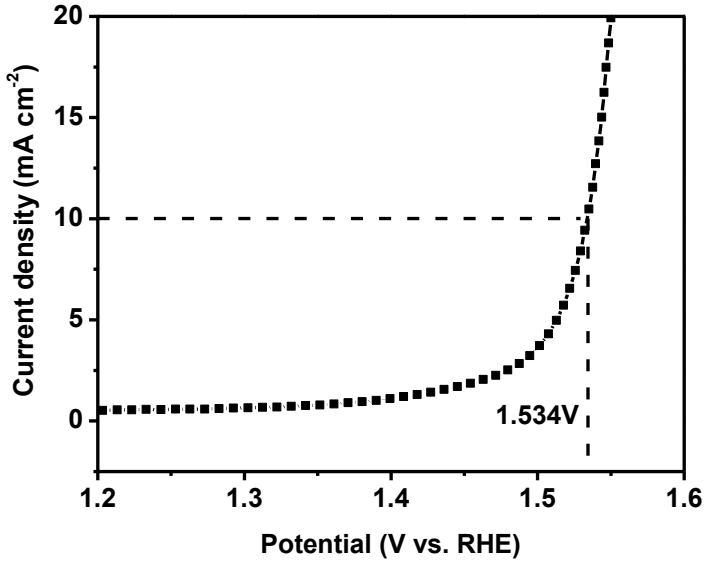

Figure S10. OER activity of $CoSe_2$@DG hybrid catalysts in 0.1 M KOH solution, related to Figure 2.
OER LSV curve of $CoSe_2$@DG hybrid catalysts in 0.1 M KOH solution.

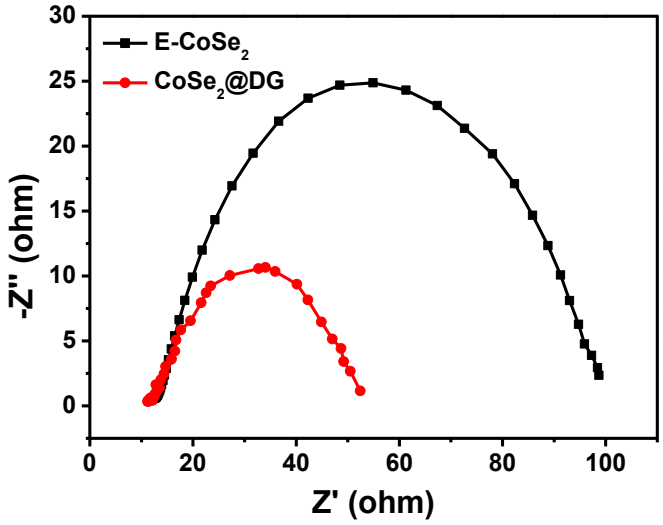

Figure S11. Impedance study of E-$CoSe_2$ and $CoSe_2$@DG, related to Figure 2.
Electrochemical impedance spectroscopy (EIS) Nyquist plots obtained at 1.33 V *vs.* RHE.

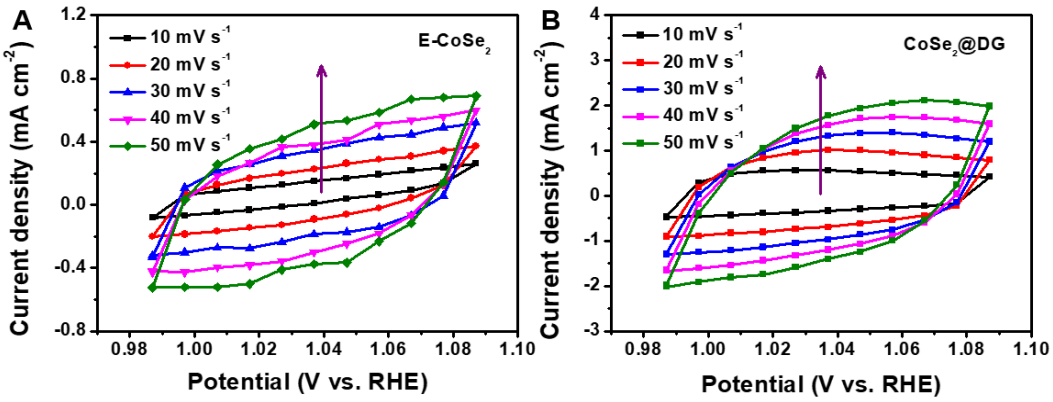

Figure S12. The electrochemical active surface areas (ECSAs) study of E-$CoSe_2$ and $CoSe_2$@DG catalysts, related to Figure 2.

Cyclic voltammetry curves of (A) E-$CoSe_2$ and (B) $CoSe_2$@DG catalysts at different scanning rate.

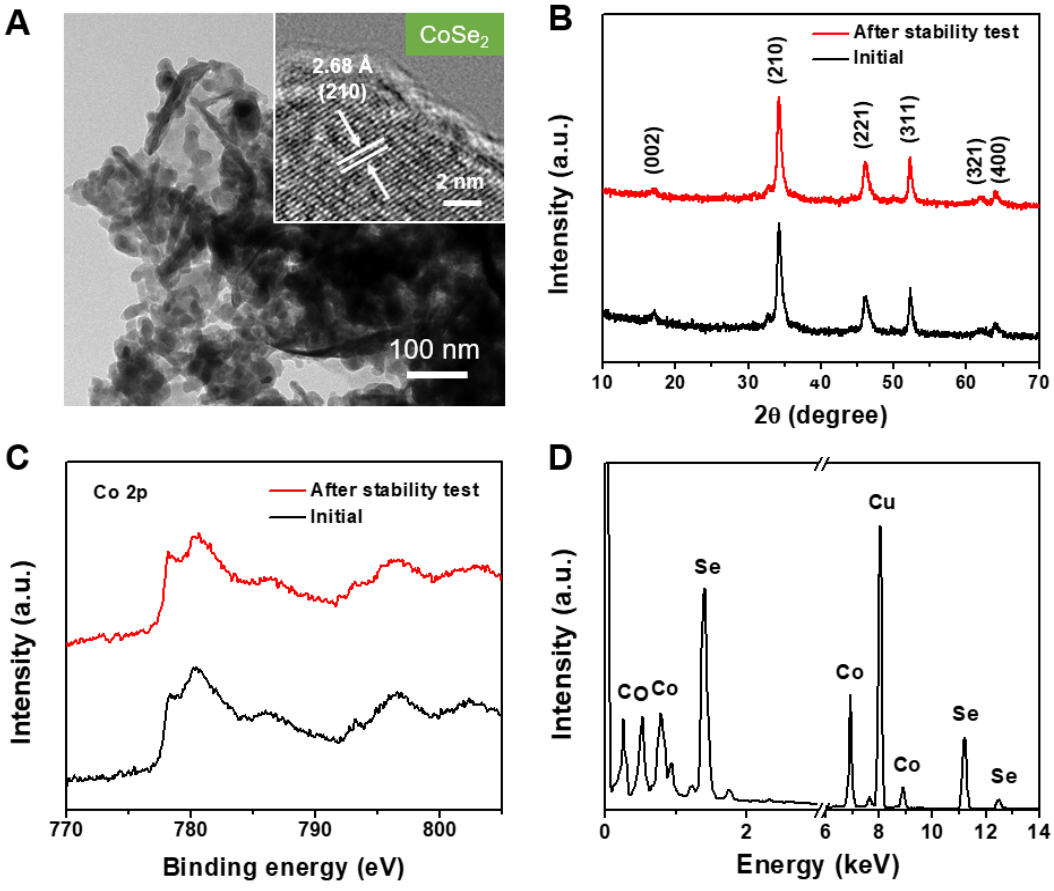

Figure S13. Characterization of $CoSe_2$@DG catalysts after continuous amperometric i-t measurement, related to Figure 2.

(A) TEM image, Inset: HRTEM image, (B) XRD patterns, (C) Co 2p XPS spectra, and (D) EDX spectrum.

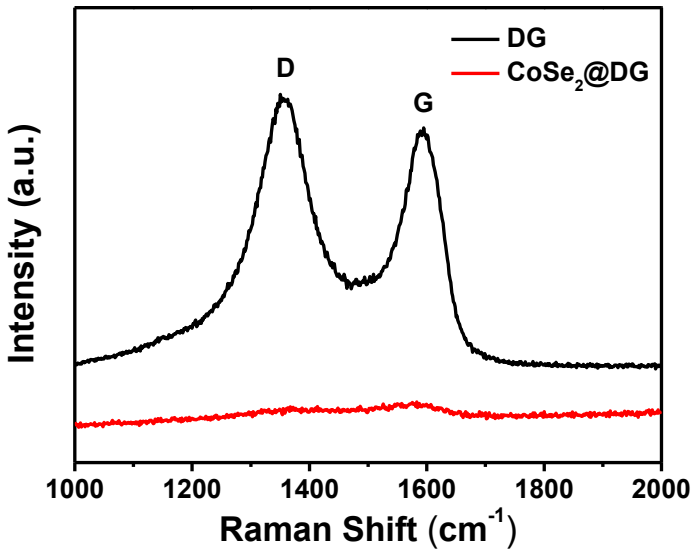

Figure S14. The study on the interaction between $CoSe_2$ and DG support, related to Figure 3.
Raman spectra of pure DG and as-prepared $CoSe_2$@DG composites.

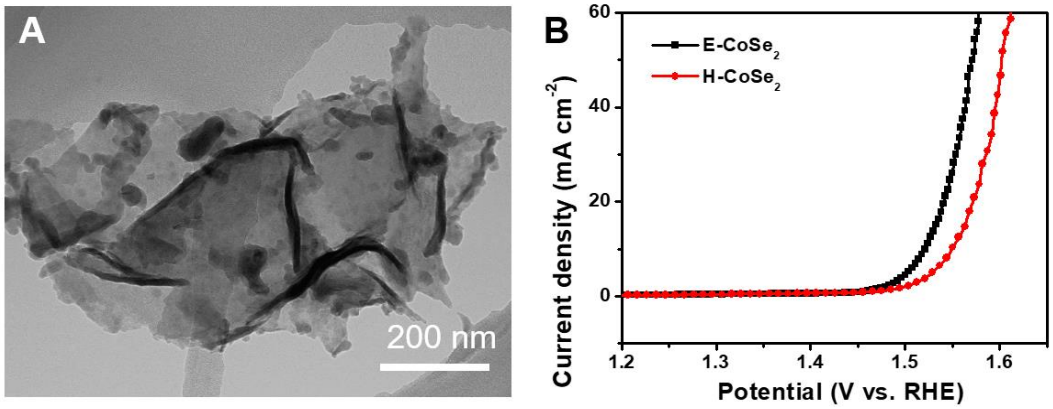

Figure S15. Characterization and OER activity of hydrothermal treated $CoSe_2$ (H-$CoSe_2$) without DG, related to Figure 3.
(A) TEM image of H-$CoSe_2$; (B) OER LSV curves of E-$CoSe_2$ and H-$CoSe_2$ samples.

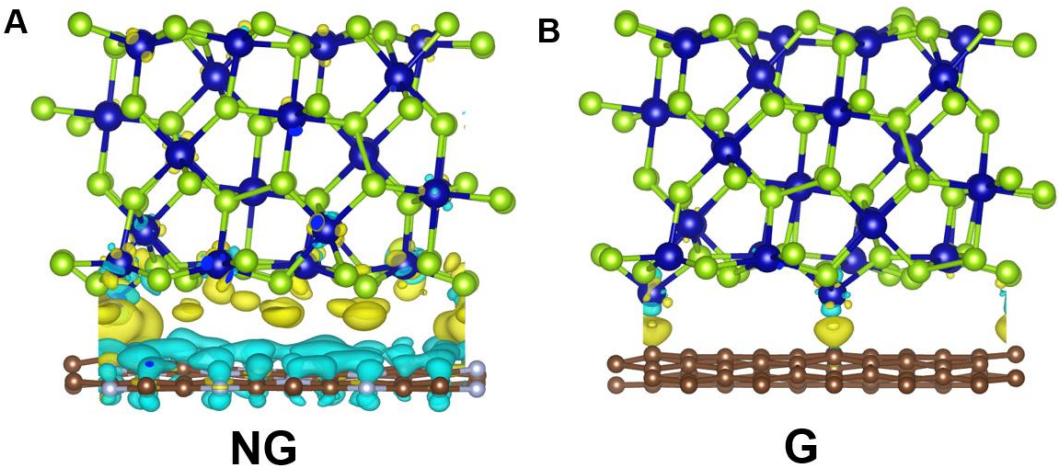

Figure S16. Charge density distribution of $CoSe_2$@NG and $CoSe_2$@G, related to Figure 4.
The side views of 3D charge density difference plot for the interfaces between graphene sheets (A for NG and B for G) and $CoSe_2$ layer calculated by DFT. Yellow and cyan isosurfaces represent charge accumulation and depletion in the 3D space with an isosurface value of 0.002 e $Å^{-3}$. Brown, green and blue balls represent C, Se and Co atoms, respectively.

Supplemental Table

Table S1. Electrocatalytic OER performance of our synthesized $CoSe_2$@DG hybrid catalysts compared with that of reported other non-precious metal electrocatalysts tested in alkaline solution, related to **Figure 2**.

Material	Electrolyte	η@10 mA cm^{-2} (mV)	*j*@350 mV (mA cm^{-2})	Tafel slope (mV dec^{-1})	Reference
$CoSe_2$@DG	**1M KOH 0.1M KOH**	**270 304**	**129 >20**	**64 N/A**	**This work**
$CoSe_2$ ultrathin nanosheets	0.1M KOH	320	<20	44	(Liu et al., 2014)
Metallic single-unit-cell $CoSe_2$ sheets	1M KOH	~340	<15	64	(Liang et al., 2015)
$CoSe_2$/CF	1M KOH	297	<50	41	(Sun et al., 2016)
$CoSe_2$/N-graphene	0.1M KOH	366	<10	40	(Gao et al., 2014)
CeO_2/$CoSe_2$	0.1M KOH	288	N/A	44	(Zheng et al., 2015)

Au nanoclusters/$CoSe_2$	0.1M KOH	410	<5	N/A	(Zhao et al., 2017)
Ag-$CoSe_2$	0.1M KOH	320	22.36	56	(Zhao et al., 2017)
$NiSe_2$ nanosheets	1M KOH	330	16.3	80	(Chen et al., 2017)
(Ni,Co)Se_2-GA	1M KOH	250	>100	70	(Xu et al., 2017)
$CoTe_2$	0.1M KOH	357	<20	32	(Gao et al., 2017)
N-doped CoS_2	1M KOH	240	~150	98	(Hao et al., 2017)
Fe-CoOOH/G	1M KOH	330	~30	37	(Han et al., 2017)
CoFe LDHs-Ar	1M KOH	266	N/A	37.85	(Wang et al., 2017)

Transparent Methods

Synthesis of $CoSe_2$-DETA lamellar nanohybrids

In a typical procedure, 2 mmol (0.498 g) of $Co(Ac)_2 \cdot H_2O$ was added into 26.0 mL of deionized water (DIW) under magnetic stirring. About 10 min later, 2 mmol (0.346 g) of Na_2SeO_3 and 52.0 mL of diethylenetriamine (DETA) were added. After stirring for 0.5 h in a beaker, the wine homogeneous solution was transferred into a 100 mL Teflon-lined autoclave, which was sealed and maintained at 180 ^oC for 16 h and then naturally cooled down to room temperature. The resulting solid product was collected and washed with absolute ethanol for 3 times to remove ions and possible remnants, and dried under vacuum at 60 ^oC for 16 h.

Exfoliation of $CoSe_2$-DETA lamellar nanohybrids

20 mg of $CoSe_2$-DETA product was dispersed in 40 mL of ethanol and then ultrasonicated in ice-water for 12 h. After ultrasonic treatment, the resultant dispersions were centrifuged at 9500 rpm for 10 min to remove the unexfoliated component. The supernatant is denoted as the exfoliated $CoSe_2$ nanosheet (E-$CoSe_2$) solution.

Synthesis of N doped graphene (NG) and defective graphene (DG)

Typically, the monolayer pristine graphene was mixed with melamine (mass ratio was 1:1), and annealed at 700 ^oC for 2 hours with a heating rate of 5 ^oC min^{-1} under nitrogen to prepare the NG. Before heating, two hours nitrogen gas flowing was needed to remove oxygen in the furnace tube. Then to prepare DG, NG was annealed at 1150 ^oC for 2 hours with a heating rate of 5 ^oC/min under nitrogen so as to subtract the nitrogen atom from the sample.

Synthesis of the $CoSe_2$@DG composite

Typically, a designed volume of DG, NG or G nanosheet (0.1 g L^{-1}) was added drop by drop into the exfoliated $CoSe_2$-NS solution under continuous stirring (the mass ratio of exfoliated $CoSe_2$ ultrathin

nanosheets and DG is 9:1). The solution was transferred into a 100 mL Teflon-lined autoclave, sealed and maintained at 60 °C for 12 h, and then naturally cooled to room temperature. The resulting product was separated by centrifugation.

Materials characterization

The samples were characterized by different analytic techniques. X-ray diffraction (XRD) patterns (2θ, 8-90°) were recorded on a Bruker D8-Advanced X-ray diffractometer using nickel-filtered Cu-Kα radiation. Electron microscope images were collected on a JEOL JSM-7001F scanning electron microscopy (SEM) at an acceleration voltage of 10 kV and a Tecnai 20 FEG transmission electron microscope (TEM) operated at 200 kV. X-ray photoelectron spectra were acquired on a Kratos Axis ULTRA X-ray photoelectron spectrometer (XPS) incorporating a 165 mm hemispherical electron energy analyser and a monochromatic Al Kα (1486.6 eV) radiation at 150 W (15 kV, 10 mA). The binding energies were determined using the C1s line at 284.6 eV from adventitious carbon as a reference. Raman spectra were recorded on a Renishaw InVia spectrometer using the 514 nm laser excitation. Thermogravimetric analysis (TGA) was carried out on a TA Instrument under air at a heating rate of 10 °C min^{-1}. The thickness of $CoSe_2$-NS was analysed by a Cypher (Asylum Research) atomic force microscope (AFM), whose cantilevers were HA_NC (Etalon) from NT-MDT, having a nominal spring constant of 4.5 N/m and nominal resonant frequency of 145 kHz. Before the AFM test the sample was dissolved in ethanol, centrifuged at 6000 rpm, and the liquid supernatant was diluted by 600 times, then dropped upon the mica plate.

Electrochemical measurements

All the electrochemical tests were performed in a conventional three-electrode system at an electrochemical station (Biologic VMP2/Z multichannel potentiostat), using Pt wire as counter electrode, glassy carbon electrode as working electrode, and an Ag/AgCl (3 M NaCl) electrode as reference electrode. For the preparation of $CoSe_2$ thin film electrode, 5 mg of catalyst powder was dispersed in 1 mL of 3:1 (v/v) DIW/2-propanol mixed solvent with 40 μL of Nafion solution (5 wt%), and then the mixture was ultrasonicated for about 1 h to generate a homogeneous ink. Next, 5.0 μL of the dispersion was transferred onto the glassy carbon disk, leading to the catalyst loading of 0.196 mg cm^{-2}. Finally, the as-prepared catalyst film was dried at room temperature. Linear sweep voltammetry (LSV) was performed at a continuous rotating speed of 1,600 rpm and a sweep rate of 5 mV/s. To assess the long-term electrocatalytic stability of $CoSe_2$@DG electrodes, the continuous amperometric i-t measurement was employed under a constant overpotential of 305 mV. The electrochemical impedance spectroscopy (EIS) measurement was carried out in the same configuration at room temperature with a sinusoidal voltage amplitude of 10 mV. The electrochemically active surface areas (ECSA) was determined by CV at the potential window 0.987 – 1.087 V (*vs.* RHE), with different scanning rate of 10, 20, 30, 40, and 50 mV/s. By plotting the difference between the anodic and cathodic current densities ($\Delta j = j_a - j_c$) at 1.037 V (*vs.* RHE) against the scan rates, the resulting linear slope is twice of the double layer capacitance (C_{dl}), which can be used to represent ECSA. The turnover frequency (TOF) value is calculated according to the following equation:

$$TOF = (J \times A) / (4 \times F \times n)$$

where J is the current density at a given overpotential (270 mV for our work), A is the surface area of the electrode (0.126 cm^2), the number of 4 represents 4 electrons/mol of O_2, F is the Faraday constant (96485.3 C/mol), and n stands for the number of moles of Co ions in as-made $CoSe_2$@DG, $CoSe_2$@G, $CoSe_2$@NG composites. In our case, all Co element was assumed to be catalytically active no matter whether they are

accessible to the electrolyte or not. Therefore, the calculated TOF value represents the lowest limit.

RHE calibration: In the all electrochemical tests, Ag/AgCl (3M NaCl) was used as the reference electrode. It was calibrated with regard to RHE. The calibration was performed in a H_2-saturated 1 M KOH electrolytes with a Pt-wire as the working electrode. CV curve was obtained at the scan rate of 1 mV s^{-1}, and the average potential at which the current crossed zero was regard as the thermodynamic potential for the hydrogen electrode reaction. The CV curve was shown as below:

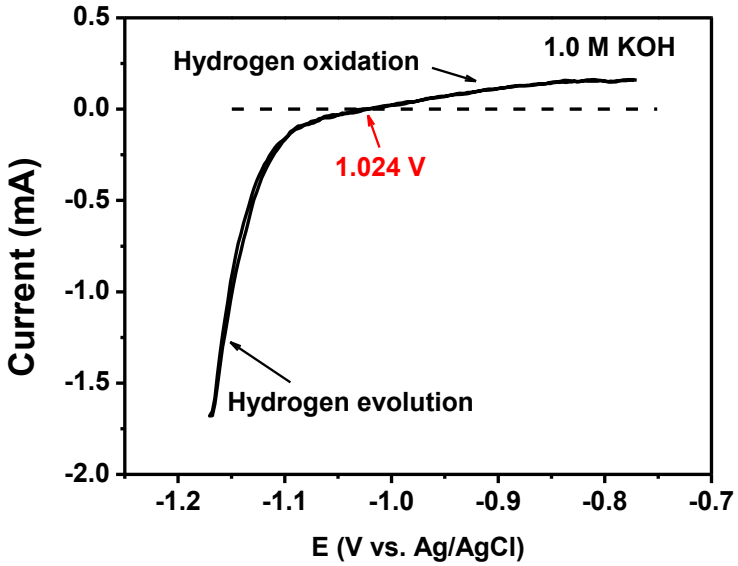

In 1 M KOH solution, all potentials were referenced to reversible hydrogen electrode (RHE) by following calculations: E (RHE) = E (Ag/AgCl) + 1.024 V.

Computational details

Density functional theory (DFT) as implemented in the Vienna Ab-initio Simulation Package (VASP) code were employed to perform the calculations (Kresse and Furthmüller, 1996a, 1996b). We use the generalized gradient approximation (Perdew et al., 1996) in the form of the Perdew–Burke–Ernzerhof functional (Perdew et al., 1996) to describe exchange-correlation interactions. Blöchl's all-electron, frozen-core projector augmented wave (PAW) method (Blöchl, 1994) was used to represent nuclei and core electrons. In all calculations, the van der Waals interaction was described by using the empirical correction in Grimme's scheme, i.e., DFT+D3 (Grimme, 2006). The Brillouin zone is sampled by gamma point. The electron wave functions were expanded using the plane waves with a cut off energy of 500 eV.

Supplemental References

Kresse, G., Furthmüller, (1996) Efficiency of ab-initio total energy calculations for metals and semiconductors using a plane-wave basis set. J., Comp. Mater. Sci. *6*, 15-50.

Kresse, G., Furthmüller, J., (1996) Efficient iterative schemes for *ab initio* total-energy calculations using a plane-wave basis set. Phys. Rev. B *54*, 11169.

Perdew, J. P., Burke, K., Ernzerhof, M., (1996) Generalized gradient approximation made simple. Phys.

Rev. Lett. *77*, 3865.

Perdew, J. P., Ernzerhof, M., Burke, K., (1996) Rationale for mixing exact exchange with density functional approximations. J. Chem. Phys. *105*, 9982-9985.

Blöchl, P. E., (1994) Projector augmented-wave method. Phys. Rev. B *50*, 17953.

Grimme, S., (2006) Semiempirical GGA-type density functional constructed with a long-range dispersion correction. J. Comput. Chem. *27*, 1787-1799.

Liu, Y., Cheng, H., Lyu, M., Fan, S., Liu, Q., Zhang, W., Zhi, Y., Wang, C., Xiao, C., Wei, S., Ye, B., Xie, Y., (2014) Low overpotential in vacancy-rich ultrathin $CoSe_2$ nanosheets for water oxidation. J. Am. Chem. Soc. 136, 15670-15675.

Liang, L., Cheng, H., Lei, F., Han, J., Gao, S., Wang, C., Sun, Y., Qamar, S., Wei, S., Xie, Y., Metallic single-unit-cell orthorhombic cobalt diselenide atomic layers: Robust water-electrolysis catalysts. Angew. Chem. Int. Ed. 54, 12004-12008.

Sun, C., Dong, Q., Yang, J., Dai, Z., Lin, J., Chen, P., Huang, W., Dong, X., (2016) Metal–organic framework derived $CoSe_2$ nanoparticles anchored on carbon fibers as bifunctional electrocatalysts for efficient overall water splitting Nano Research 9, 2234-2243.

Gao, M.-R., Cao, X., Gao, Q., Xu, Y.-F., Zheng, Y.-R., Jiang, J., Yu, S.-H., (2014) Nitrogen-doped graphene supported $CoSe_2$ nanobelt composite catalyst for efficient water oxidation. ACS Nano 8, 3970-3978.

Zheng, Y.-R., Gao, M.-R., Gao, Q., Li, H.-H., Xu, J., Wu, Z.-Y., Yu, S.-H., (2015) An efficient CeO_2/$CoSe_2$ nanobelt composite for electrochemical water oxidation. Small 11, 182-1888.

Zhao, S., Jin, R., Abroshan, H., Zeng, C., Zhang, H., House, S.D., Gottlieb, E., Kim, H.J., Yang, J.C., Jin, R., (2017) Gold nanoclusters promote electrocatalytic water oxidation at the nanocluster/$CoSe_2$ interface. J. Am. Chem. Soc. 139, 1077-1080.

Zhao, X., Zhang, H., Yan, Y., Cao, J., Li, X., Zhou, S., Peng, Z., Zeng, J., (2017) Engineering the electrical conductivity of lamellar silver-doped cobalt(ii) selenide nanobelts for enhanced oxygen evolution. Angew. Chem. Int. Ed. 56, 328-332.

Chen, S., Kang, Z., Hu, X., Zhang, X., Wang, H., Xie, J., Zheng, X., Yan, W., Pan, B., Xie, Y., (2017) Delocalized spin states in 2d atomic layers realizing enhanced electrocatalytic oxygen evolution. Adv. Mater. DOI: 10.1002/adma.201701687.

Xu, X., Liang, H., Ming, F., Qi, Z., Xie, Y., Wang, Z., (2017) Prussian blue analogues derived penroseite (Ni,Co)Se_2 nanocages anchored on 3D graphene aerogel for efficient water splitting. ACS Catal. 7, 6394-6399.

Gao, Q., Huang, C.-Q., Ju, Y.-M., Gao, M.-R., Liu, J.-W., An, D., Cui, C.-H., Zheng, Y.-R., Li, W.-X., Yu, S.-H.,(2017) Phase-selective syntheses of cobalt telluride nanofleeces for efficient oxygen evolution catalysts. Angew. Chem. Int. Ed. 27, 7877-7881.

Hao, J., Yang, W., Peng, Z., Zhang, C., Huang, Z., Shi, W., (2017) A nitrogen doping method for CoS_2 electrocatalysts with enhanced water oxidation performance. ACS Catal. 7, 4214-4220.

Han, X., Yu, C., Zhou, S., Zhao, C., Huang, H., Yang, J., Liu, Z., Zhao, J., Qiu, J., (2017) Ultrasensitive iron-triggered nanosized Fe-CoOOH integrated with graphene for highly efficient oxygen evolution. Adv. Energy Mater. DOI: 10.1002/aenm.201602148.

Wang, Y., Zhang, Y., Liu, Z., Xie, C., Feng, S., Liu, D., Shao, M., Wang, S., (2017) Layered double hydroxide nanosheets with multiple vacancies obtained by dry exfoliation as highly efficient oxygen

evolution electrocatalysts. Angew. Chem. Int. Ed. 27, 5961-5965.